



Shahid Chamran
University of Ahvaz

Journal of Applied and Computational Mechanics



Research Paper

How Wavelike Bumps Mitigate the Vortex-induced Vibration of a Drilling Riser

Liping Tang¹, Hong Yao¹, Zemin Huang², Liqi Wang¹, Xiaohua Zhu¹

¹ School of Mechatronic Engineering, Southwest Petroleum University, Chengdu, 610500, P.R. China

² China Petroleum Pipeline Engineering Corporation, Langfang, 065000, P.R. China

Received September 10 2020; Revised January 03 2021; Accepted for publication January 30 2021.

Corresponding authors: Liping Tang (lipingtang@swpu.edu.cn); Xiaohua Zhu (zhuxh@swpu.edu.cn)

© 2021 Published by Shahid Chamran University of Ahvaz

Abstract. In this paper, computational fluid dynamics is used to study how wavelike bumps influence the suppression of drilling-riser vortex-induced vibration (VIV). The numerical model involves two-dimensional unsteady incompressible turbulent flow around a cylinder, with the flow characteristics regarded as being constant. The results show that wavelike bumps are effective in mitigating the VIV, but the degree of mitigation does not increase indefinitely with the number of bumps. The mitigation is greatest with either 5 or 7 wavelike bumps, reducing the vibration amplitudes of the cylinder in the in-line and cross-flow directions to negligible levels. To know how equipping a circular cylinder with wavelike bumps affected its VIV response, cases with wavelike bumps of 1, 3, 5, 7, 9, and 11 are studied.

Keywords: Vortex-induced vibration, Wavelike bumps, Reduced velocity, Frequency spectrum, Suppression effect.

1. Introduction

Vortices form when a fluid flows around a bluff body, thereby changing the pressure distribution along the body surface. If the vortices are not located symmetrically around the body, then lift and drag are generated, thereby leading to flow-induced structural vibration [1]. If the vortex shedding frequency is close to the natural frequency of the structure in question, then the structure can experience large-amplitude vibration in a type of motion known as vortex-induced vibration (VIV) [2]. In particular, the VIV of circular cylinders is a subject of academic and industrial research because of its theoretical and applied importance [3]. Meanwhile, risers and pipes are widely used in many industrial and mechanical applications and devices [4], such as to develop offshore energy. For manufacturing convenience and structural stability, ocean engineering tends to involve cylindrical structures such as the drilling and production risers of drilling platforms and the cables of production operations [5]. VIV is a primary source of fatigue damage for slender offshore structures [6-8], thereby making it very important to investigate the VIV of drilling risers and pipes used in offshore oil and gas development.

Investigations started by Fernandes et al. [9] showed that VIV can appear in still water if the riser moves because of the vertical harmonic motion of the platform, meaning that platform motion can also lead to riser vibration. Fernandes et al. showed that a submerged riser can experience transverse VIV due to cylinder self-vibration caused by wave-induced platform motion; they termed such motion vortex self-induced vibration and carried out experimental investigations to verify their experimental studies [10]. By regarding a flexible riser as an Euler beam and using an inverse method to calculate the hydrodynamic forces, Song et al. [11] obtained the hydrodynamic characteristics of a flexible riser encountering VIV in a uniform flow; their results provide a reference for simulating riser hydrodynamics numerically. Many VIV studies consider a horizontal cylinder, where pretension acting perpendicular to the distributed weight of the cylinder is included [12, 13]. However, a detailed consideration of the vertical configuration shows that the weight distribution is an important factor. By considering the weight distribution, Pavlovskaya et al. [14] compared the multi-mode dynamics of vertical and horizontal risers.

Cylinder VIV has been subjected to comprehensive numerical investigation in previous studies. Chen et al. [15] studied how top-end vertical motion affects riser VIV and found that (i) the dynamic displacement of the riser increases greatly when top-end motion is included, (ii) the top-end motion becomes more influential with decreasing mode number, and (iii) the natural dynamic characteristics of the slender structure cause mode transition to arise at low frequencies. Kang et al. [16] studied cylinder VIV numerically by using the Open Foam software to implement a shear-stress transport (SST) $k-\omega$ turbulence model; using various frequency and mass ratios, they showed that (i) the VIV characteristics depend on the Reynolds number and (ii) that dependence in turn depends on the combination of frequency and mass ratios. Meanwhile, there have been various examples of cylinder VIV arising near walls [17]. A series of numerical simulations were conducted involving a planar boundary and a nondimensional gap ratio $S^*=S/D$ as a parameter (where S is the distance between the wall and the cylinder tangent and D is the cylinder diameter) [18-21], including cases for $0.2 \leq S^* < 2$ and $S^* \geq 2$. Based on that work, Daneshvar and Morton [22] studied the one-degree-of-freedom (1-DOF) VIV of an elastically mounted cylinder near a wall boundary for a wide range of S^* .



In experiments on the VIV of a 2-DOF horizontal cylinder, Kang and Jia [23] found that the VIV trajectories of the cylinder depended substantially on the combination of reduced velocity and natural frequency. Sensitivity analyses are undoubtedly valuable for optimizing VIV-induced riser dynamics. Meliga et al. [24] derived the flow sensitivity of characteristics that are manifest at low Reynolds number, but such studies are currently lacking for high Reynolds number. To understand the system behavior at high Reynolds number, Jiménez-González and Huera-Huarte [25] conducted experiments to study the VIV response sensitivity at high Reynolds number, using sensitivity maps to determine the locations of the perturbing structures. To check whether the independence principle is valid for studying VIV, Seyed-Aghazadeh and Modarres-Sadeghi [26] investigated how the angle of inclination affects the VIV response. Franzini et al. [27] used a long flexible vertical cylinder to investigate experimentally the relationship between top-motion excitation and the concomitant VIV; they showed that parametric instability of the first vibration mode appears together with VIV when the top-motion excitation frequency is twice the first natural frequency.

For the field application of marine structures, one of the most important aspects is the suppression of VIV. Borges et al. [28] proposed using viscoelastic sandwich layers to suppress the VIV of steel catenary risers; they found that the viscoelastic sandwich structure reduced the VIV greatly and increased the riser lifetime. Most studies to date have involved fitting cylinders with strakes, including straight and helical strakes [29-31]. Korkischko and Meneghini [32] investigated how the geometrical parameters of helical strakes affect cylinder VIV; they considered different combinations of strake height and pitch, and they studied the dynamics of isolated and tandem cylinders. Zhu et al. [33] used sequential fluid-structure interaction to evaluate the flow-driven rotation and VIV of a cylinder, and they studied the installation of Bach-type current turbines for VIV suppression. To control the VIV response, Nikoo et al. [34] proposed a new compound passive technique in the form of a textured pipe-in-pipe structure, which was a modification of the conventional pipe-in-pipe system.

In the present paper, we investigate how wavelike bumps affect VIV suppression, focusing in particular on parametric sensitivity regarding strakes fitted to the rear of a cylinder. Computational fluid dynamics (CFD) is used as a tool to study the effect of the deflection angle, the Reynolds number and so on [35]. We use CFD to study the effects of having 0, 1, 3, 5, 7, 9, and 11 wavelike bumps in the cylindrical wake area in this paper. We regard the flow around the cylinder as being two-dimensional unsteady incompressible turbulent flow with constant flow characteristics. We use the finite-volume method to solve the two-dimensional Reynolds-averaged Navier-Stokes (RANS) equations and the SST $k-\omega$ turbulence model to simulate the turbulent flow in the wake of the circular cylinder. The results show that having wavelike bumps in the wake area is an effective way to suppress the VIV. However, the degree of suppression does not increase indefinitely with the number of bumps, with 5 or 7 bumps being most effective.

2. Numerical method and model

2.1 Governing equations

2.1.1 Flow equations

Wanderley et al. [36] showed that a two-dimensional model based on the RANS equations can capture cylinder VIV. In the present study, we consider the flow around the cylinder as being two-dimensional unsteady incompressible model with constant flow characteristics and governed by the unsteady two-dimensional RANS equations. Because the flow around the cylinder is incompressible, the capacity for heat exchange is negligible, and thus the RANS governing equations comprise only mass and momentum conservation. The specific governing equations for incompressible viscous flow [37] are

$$\frac{\partial U_i}{\partial x_i} = 0, \quad (1)$$

$$\frac{\partial U_i}{\partial t} + (U_j - \hat{u}_j) \frac{\partial U_i}{\partial x_j} = -\frac{1}{\rho} \frac{\partial P}{\partial x_i} + \frac{\partial}{\partial x_j} \left(2\nu S_{ij} - \overline{u_i u_j} \right), \quad (2)$$

where U_i is the instantaneous velocity in the i direction (here, U_i is the mean velocity and u_i is the velocity fluctuation), P is the instantaneous pressure (here, P is the mean pressure and p' is the pressure fluctuation), t is time, \hat{u}_j is the mesh velocity, ρ is the fluid density, ν is the kinematic viscosity, S_{ij} is the mean strain tensor, and $\overline{u_i u_j}$ is the average product of fluctuating velocities.

2.1.2 Turbulence model

Because the continuity and RANS equations are not closed, we require a turbulence model. Herein, we use a modified SST $k-\omega$ turbulent energy model [16] that performs RANS closure while offering good predictions of boundary-layer flow under a counter gradient. The turbulence model is expressed as

$$\frac{\partial \rho k}{\partial t} + u_j \frac{\partial \rho k}{\partial x_j} = P_k - \beta^* \rho k \omega + \frac{\partial}{\partial x_j} \left[\left(\mu + \sigma_k \mu_t \right) \frac{\partial k}{\partial x_j} \right], \quad (3)$$

$$\frac{\partial \rho \omega}{\partial t} + u_j \frac{\partial \rho \omega}{\partial x_j} = P_\omega - \beta \rho \omega^2 + \frac{\partial}{\partial x_j} \left[\left(\mu + \sigma_\omega \mu_t \right) \frac{\partial \omega}{\partial x_j} \right] + 2\rho (1-F_1) \left[\sigma_{\omega 2} \frac{1}{\omega} \frac{\partial k}{\partial x_j} \frac{\partial \omega}{\partial x_j} + \frac{1}{2} \beta' \frac{1}{Q+k} \left| \frac{\partial(Q+k)}{\partial t} \right| P_k \right], \quad (4)$$

where k is the turbulent kinetic energy, ω is the turbulent dissipation rate, P_k and P_ω are the turbulent kinetic energy generation and dissipation rates, respectively, μ is the dynamic viscosity, μ_t is the kinetic eddy viscosity, Q is the mean flow kinetic energy per unit mass, and the parameters β , β^* , β' , σ_k , σ_ω , and $\sigma_{\omega 2}$ are obtained by optimizing numerical simulations [16].

2.1.3 Equations of motion

The cylinder undergoes self-oscillation because of fluid-solid interaction. As such, the dynamic equations for the vibration of a 2-DOF cylinder can be expressed as the following control equations [16]:



$$\ddot{x} + C_{\zeta x} \dot{x} + C_{kx} x = \frac{C_D}{2C_\mu}, \quad (5)$$

$$\ddot{y} + C_{\zeta y} \dot{y} + C_{ky} y = \frac{C_L}{2C_\mu}, \quad (6)$$

where x and y are the displacements in the in-line (IL) and cross-flow (CF) directions, respectively, (\cdot) is the derivative with respect to time, $C_{\zeta x} = C_{\zeta y} = 4\pi\xi / U_r$ are the dimensionless damping coefficients (here, ξ is the ratio of structural damping to critical damping and $U_r = U/(f_n D)$ is the reduced velocity, where f_n is the natural frequency of the structure), $C_{kx} = C_{ky} = 4\pi^2 / U_r^2$ are the dimensionless stiffness coefficients, $C_\mu = m/(\rho D^2)$ is the dimensionless mass, and $C_D = 2F_D/(\rho U^2 D)$ and $C_L = 2F_L/(\rho U^2 D)$ are the drag and lift coefficients in the IL and CF directions, respectively, where F_D and F_L are the corresponding forces acting on the cylinder in the respective directions.

2.2 Numerical model and its verification

2.2.1 Numerical model

A Figure 1(a) shows the 2-DOF computational model of flow around a cylinder fitted with wavelike bumps in the wake area. To ensure that the wake flow develops completely, the calculation area of the model is $20D \times 40D$ (where $D=38.1\text{mm}$ is the cylinder diameter). For the boundary conditions, the left and right boundaries are set as the velocity inlet and outlet, respectively, the upper and lower boundaries are symmetry boundaries, and the cylinder surface is a slip-free wall. Figure 1(a) shows the distances from the cylinder center to each boundary, and Figure 1(b) shows an enlarged view of the wavelike bumps at the rear of the cylinder; for a given wavelike bump, the diameter d is 5.6mm , the height h is 1.905mm , and the central angle corresponding to the height is 150° (see Fig. 1(b)). The first wavelike bump is located at the center of the cylinder rear; for 3 bumps, we add two more on either side of the first, and so on. Herein, we analyze what happens with 1, 3, 5, 7, 9, and 11 wavelike bumps.

2.2.2 Mesh generation and iteration

As shown in Fig. 2(a), we use moving-mesh adjustment in a circle of radius $3D$, for which we use the arbitrary Lagrangian-Eulerian technique. With this technique, the domain mesh can move arbitrarily to optimize the element shapes, while the interface and boundary meshes can move along with materials to trace the interfaces and boundaries. Herein, we use the SST $k-\omega$ turbulence model, and we refine the mesh near the wall surface to ensure accurate solution of the viscous bottom layer. The mesh of the first layer on the wall must satisfy $y^+ \approx 1$. The near-wall mesh is shown in Fig. 2(b), where y^+ is defined as:

$$y^+ = 0.172 \frac{\Delta y}{L} \text{Re}^{0.9}, \quad (7)$$

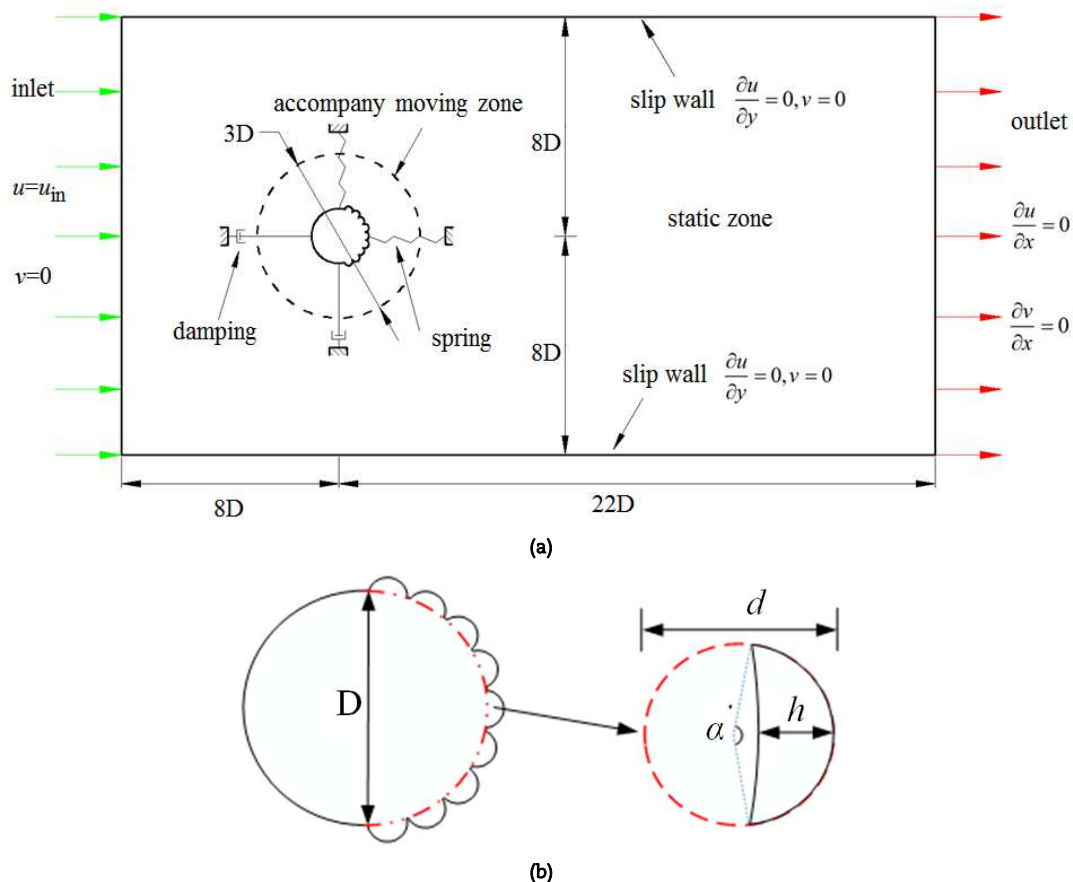


Fig. 1. Computational domain for vortex-induced vibration (VIV) of a circular cylinder: (a) computational domain; (b) details of wavelike bumps on cylinder.



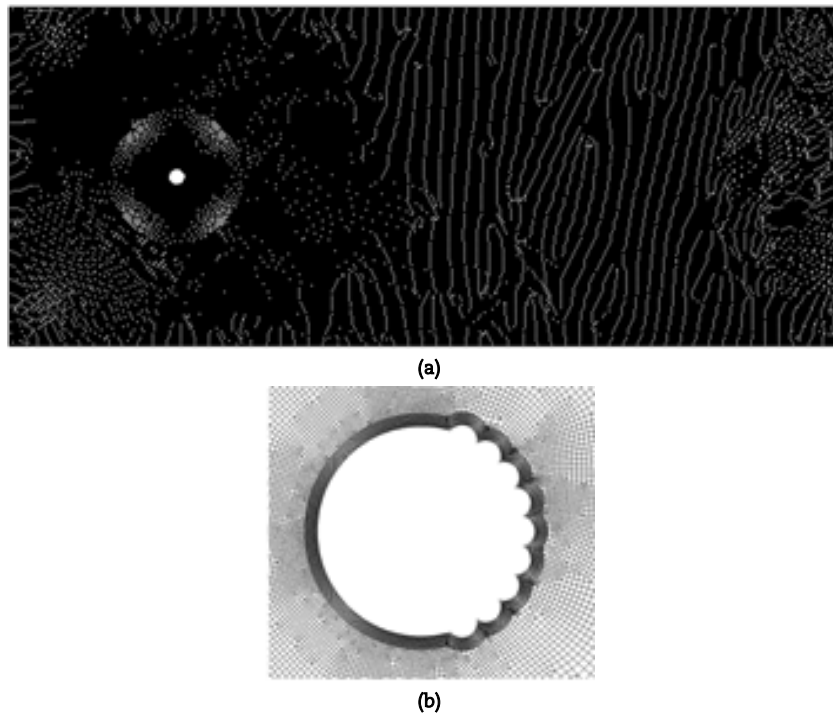


Fig. 2. Computational meshes used for numerical simulation: **(a)** entire mesh system; **(b)** mesh near wavelike bumps on circular cylinder.

where Δy is the distance between the first inner node and the wall surface, L is the characteristic length of the cylinder, and Re is the Reynolds number.

By regarding the cylinder as a rigid moving particle in the x - y plane, the dynamic equations of the cylinder can be solved by referring to the nonlinear vibration of the 1-DOF particle. We use the fourth-order Runge–Kutta method to discretize and solve the dynamic equations to obtain the displacement and velocity of the cylinder at each time step. As the example here, we consider the displacement $x(t_{n+1})$ and velocity $\dot{x}(t_{n+1})$ of the cylinder in the IL direction.

$$\dot{x}(t_{n+1}) = \dot{x}(t_n) + \frac{\Delta t}{6} \times (K_{x1} + 2K_{x2} + 2K_{x3} + K_{x4}), \quad (8)$$

$$K_{x1} = \frac{F_D(t_n)}{m} - 2\zeta\omega_0\dot{x}(t_n) - \omega_0^2x(t_n), \quad (9)$$

$$K_{x2} = \frac{F_D(t_n)}{m} - 2\zeta\omega_0\left[\dot{x}(t_n) + \frac{\Delta t}{2}K_{x1}\right] - \omega_0^2\left[x(t_n) + \frac{\Delta t}{2}\dot{x}(t_n)\right], \quad (10)$$

$$K_{x3} = \frac{F_D(t_n)}{m} - 2\zeta\omega_0\left[\dot{x}(t_n) + \frac{\Delta t}{2}K_{x2}\right] - \omega_0^2\left[x(t_n) + \frac{\Delta t}{2}\dot{x}(t_n) + \frac{\Delta t^2}{4}K_{x1}\right], \quad (11)$$

$$K_{x4} = \frac{F_D(t_n)}{m} - 2\zeta\omega_0[\dot{x}(t_n) + \Delta t K_{x3}] - \omega_0^2\left[x(t_n) + \dot{x}(t_n)\Delta t + \frac{\Delta t^2}{2}K_{x2}\right], \quad (12)$$

where K_{x1} , K_{x2} , K_{x3} , and K_{x4} are the transformation equations, Δt is the time step, and the subscript n is the number of time steps.

Knowing the displacement $x(t_n + 1)$ and velocity $\dot{x}(t_n + 1)$ at time step t_n , we use Eqs.(8)–(12) to calculate the displacement and velocity at the next time step $t_{n+1} = t_n + \Delta t$. The displacement and velocity of the cylinder in the CF direction are solved in the same way as are those in the IL direction; we simply change the velocity $\dot{x}(t_n + 1)$ to $\dot{y}(t_n + 1)$ and the displacement $x(t_n + 1)$ to $y(t_n + 1)$. For the calculation, the boundary conditions of the cylinder surface are set as

$$x(t_0) = 0, y(t_0) = 0, \quad (13)$$

$$\dot{x}(t_0) = u(t_0) = 0, \dot{y}(t_0) = v(t_0) = 0, \quad (14)$$

2.2.3 Model verification

To assess the feasibility of the present numerical simulation model, we used the same parameter values as those in the experiments by Jauvtis and Williamson [38]. Figure 3 shows the relationship between the vibration amplitude and the reduced velocity; in general, the numerical results agree with the experimental responses, but the lateral amplitude moves slightly toward smaller reduced velocity. A plausible interpretation for this discrepancy is that the experiments involve a turbulent-convection hysteresis phenomenon that does not arise in the simulation.



3. Results and discussion

3.1 Vibration suppression

The vibration amplitude is one of the most important factors with which to evaluate the VIV suppression effect. Figure 4 shows the relationships between amplitude response and reduced velocity for both a smooth cylinder and one with wavelike bumps. As can be seen, the wavelike bumps are good at suppressing the transverse vibration of the cylinder, but the amplitude reduction is gentle when the reduced velocity of the cylinder with wavelike bumps is in the range of 2–12. Rather than increasing indefinitely with the number n of wavelike bumps, the degree of suppression is best with $n=9$. For $n=5$, the lateral amplitude response of the cylinder is close to that of the smooth cylinder, indicating that the suppression effect is not ideal in that case.

According to the results in Fig. 4., being different from the smooth cylinder, the cylinder with wavelike bumps has a maximum amplitude corresponding to a reduced velocity U_r that is no longer $U_r=6$. Different values of maximum dimensionless amplitude $A_y=X/D$ and U_r are obtained for different numbers of wavelike bumps: $A_y=0.642$ and $U_r=8$ for $n=1$; $A_y=0.654$ and $U_r=8$ for $n=3$; $A_y=1.047$ and $U_r=6$ for $n=5$; $A_y=0.825$ and $U_r=6$ for $n=7$; $A_y=0.167$ and $U_r=12$ for $n=9$; and $A_y=0.482$ and $U_r=6$ for $n=11$. The drag force increases with increasing cross-sectional area of the cylinder, leading to increasing amplitude of the cylinder in the IL direction. For $n=11$, the maximum amplitude in the flow direction is $0.197D$ at $U_r=6$. For $n=7$, the maximum amplitude reaches its maximum value of $0.1485D$ at $U_r=9$. For the other values of n , the maximum amplitude of the cylinder in the flow direction seems to respond similarly to that of the smooth cylinder, but with different values of U_r .

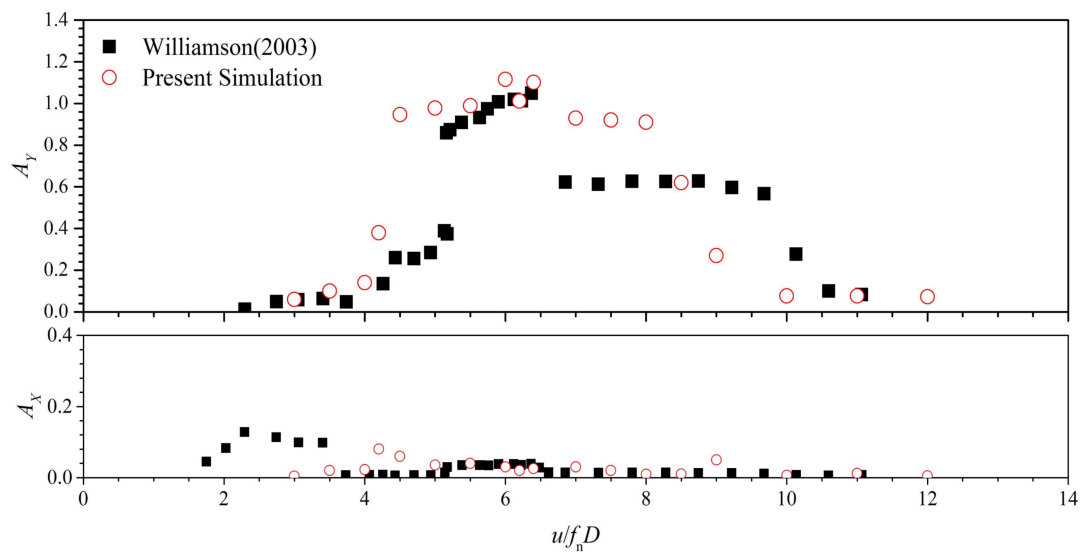


Fig. 3. Comparison of amplitude responses between computational simulation results and experiments by Jauvtis and Williamson [38].

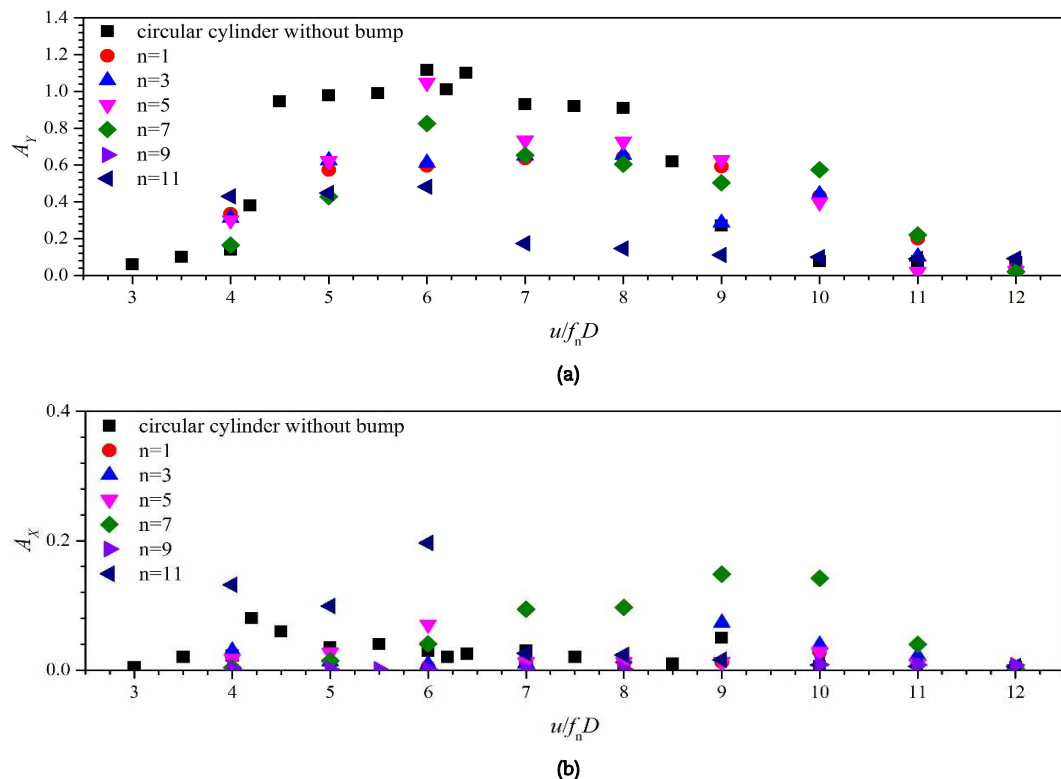


Fig. 4. Non-dimensional amplitude at different values of reduced velocity: (a) cross-flow (CF) direction; (b) in-line (IL) direction.



3.2 Dynamic trajectory

The dynamic trajectory is another important aspect for judging how wavelike bumps influence cylinder VIV suppression. Also seen clearly in the trajectory figures are the vibration type and the dynamic response. Figure 5 shows the dynamic trajectories of the smooth cylinder and the cylinders with different numbers of wavelike bumps at different reduced velocities.

Figure 5(a) shows the dynamic trajectory of the smooth cylinder for different values of U_r . As can be seen, the dynamic trajectory of the smooth cylinder is irregular for $U_r = 4$. For $U_r = 4.5-8$, the dynamic trajectories have a figure-of-eight shape and the dimensionless amplitudes Y/D in the CF direction are around 1.0, indicating that the vibration of the smooth cylinder in the CF direction is in the “locked area”. With increasing U_r , the dimensionless amplitude X/D in the IL direction increases from 0.1 to 0.25 and the dynamic trajectory becomes oblate for $U_r = 10$ and tends to a small cluster at $U_r = 12$. For $U_r = 10$, the maximum amplitudes in the CF and IL directions are approximately 0.5 and 0.55, respectively. For $U_r = 12$, the CF vibration amplitude decreases considerably to 0.2 and the IL one reaches approximately 0.4.

Figure 5(b) shows the dynamic trajectory of the cylinder with 1 wavelike bump for different values of U_r . For $U_r = 4, 5$, and 6, the dynamic trajectory of the cylinder has the shape of an inverted water droplet. With an increase in U_r , the CF vibration amplitude increases from 0.6 to approximately 1.0. For $U_r = 7-12$, the dynamic trajectory of the cylinder is irregularly shaped and the CF vibration amplitudes are all approximately 0.3. In general, the IL vibration amplitude increases from 0.08 to 0.23 with increasing U_r .

Figure 5(c) shows the dynamic trajectories of the $n=3$ cylinder for different values of U_r . As can be seen, the dynamic trajectories are irregular except for the one for $U_r = 7$, which has a figure-of-eight shape.

Figure 5(d), (e) show the dynamic trajectories of the $n=5$ and 7 cylinders, respectively, for different values of U_r . With increasing U_r , the IL vibration amplitude increases. In all cases, however, both the IL and CF vibration amplitudes are very small, indicating that the VIV has been mitigated substantially.

Figure 5(f) shows the dynamic trajectories of the $n=9$ cylinder for different values of U_r . As can be seen, the dynamic trajectory has a figure-of-eight shape for $U_r = 4-8$. In these cases, the maximum CF and IL vibration amplitudes are approximately 0.15 and 0.17, respectively. For $U_r = 10$ and 12, the dynamic trajectory changes from a figure of eight to irregular.

Figure 5(g) shows the dynamic trajectories of the $n=11$ cylinder for different values of U_r . For each U_r , the dynamic trajectory is elliptical.

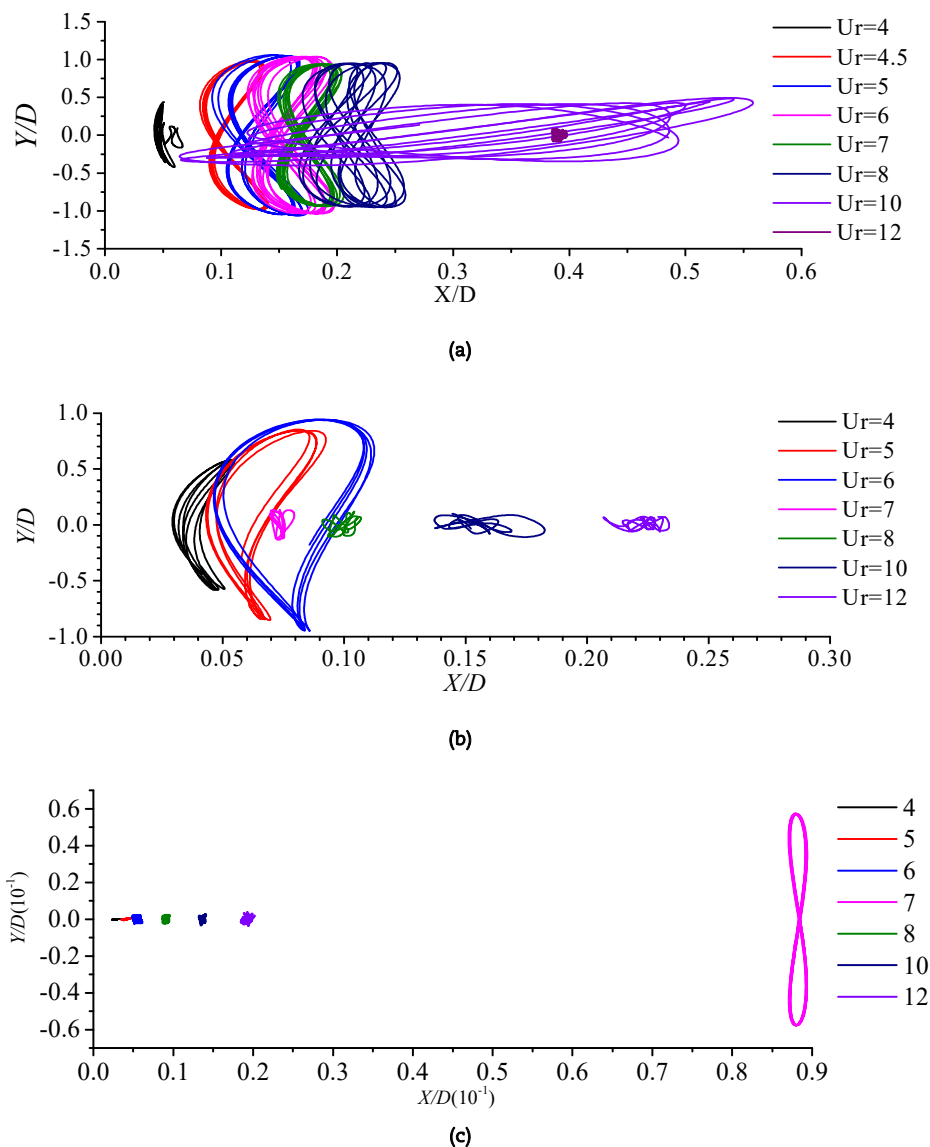


Fig. 5. Dynamic trajectories of cylinder with different number n of wavelike bumps at different reduced velocities: n = (a) 0, (b) 1, (c) 3, (d) 5, (e) 7, (f) 9, and (g) 11.



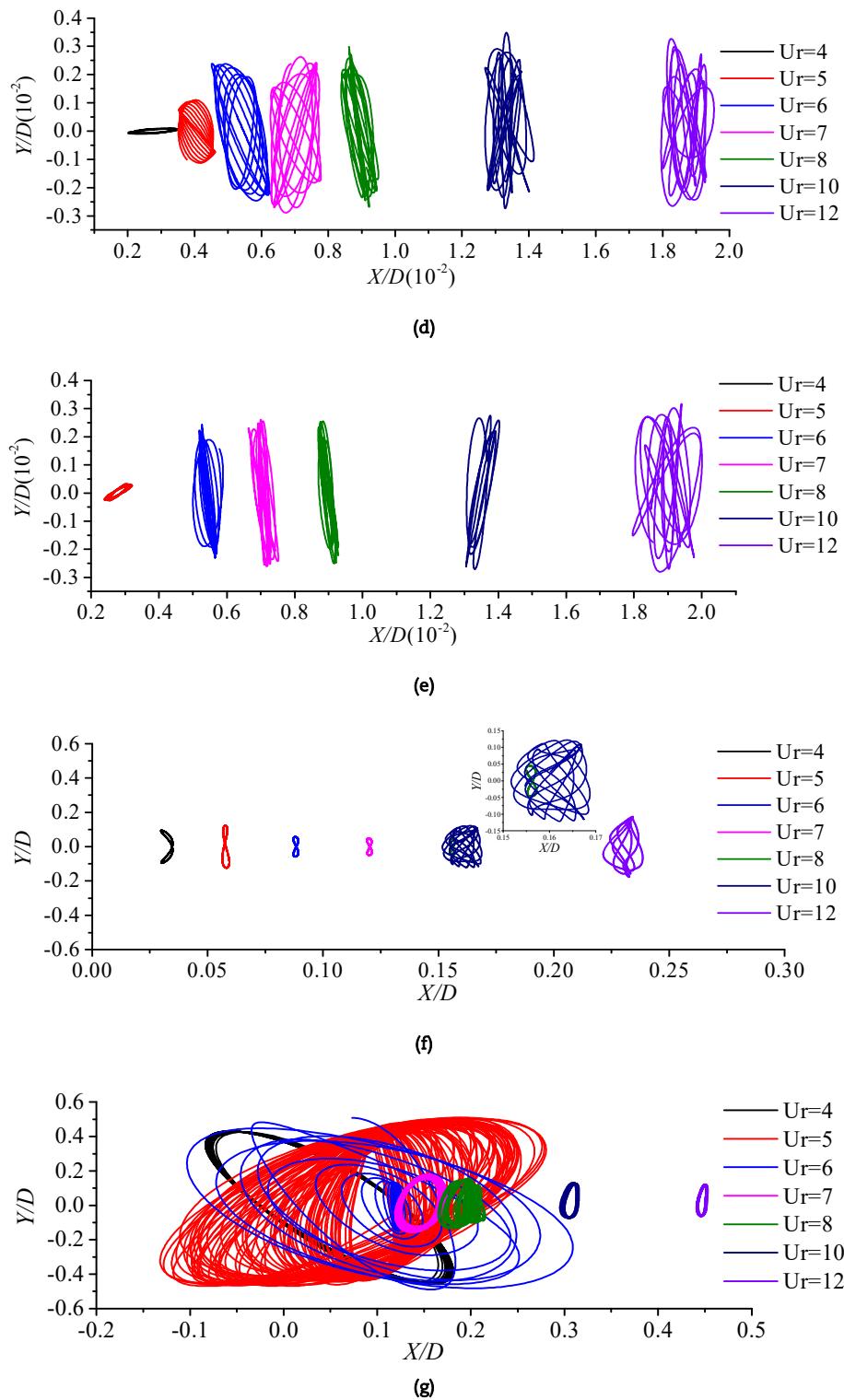


Fig. 5. Continued.

3.3 Amplitude and frequency spectrum of VIV response

Figure 6 shows the amplitude response and frequency spectrum of the cylinder with different values of n . Figure 6(a) shows the dynamic response of the smooth cylinder ($n=0$). For $n=1$ (Fig. 6(b)), the CF vibration amplitude decreases from $A_V = 0.4$ to approximately 0.05 with increasing U_r . For $n=3$ (Fig. 6(c)), the CF vibration amplitude increases first and then decreases with increasing U_r ; we have $f_{sx}/f_{sy} = 1$ when $U_r = 4$, indicating that the dynamic trajectory of the cylinder is circular. For $n=5$ (Fig. 6(d)), A_V changes little with increasing U_r and similarly the dynamic trajectory is circular ($f_{sx}/f_{sy} = 1$) when $U_r = 4$. For $n=7$ (Fig. 6(e)), the CF vibration amplitude increases with increasing U_r ; in general, the vibration amplitude is small for the analyzed U_r cases. For $n=9$ (Fig. 6(f)), A_V remains approximately 0.15 and f_{sx}/f_{sy} remains approximately 2 for different values of U_r ; in this condition, the cylinder moves in a figure-of-eight shape, corresponding to the dynamics shown in Fig. 5(f). For $n=11$ (Fig. 6(g)), with increasing U_r , the maximum value of A_V decreases gradually from approximately 0.4 to approximately 0.1 and we have $f_{sx}/f_{sy} = 1$ for each reduced velocity; the $n=11$ cylinder moves on a relatively regular circle or ellipse, corresponding to the results in Fig. 5(g).



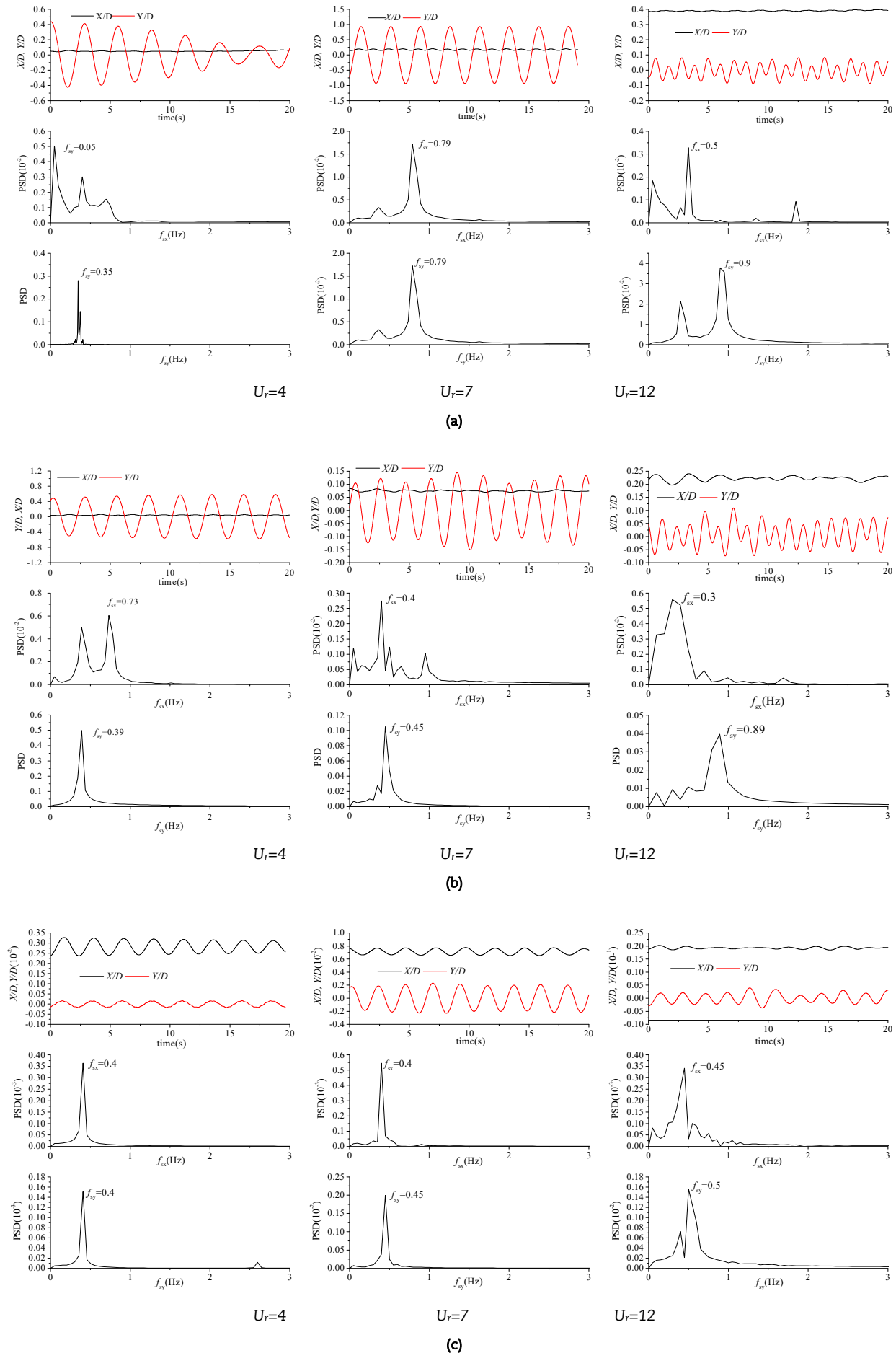


Fig. 6. Amplitude response and frequency spectrum of cylinder with different number n of wavelike bumps: n = (a) 0, (b) 1, (c) 3, (d) 5, (e) 7, (f) 9, and (g) 11.



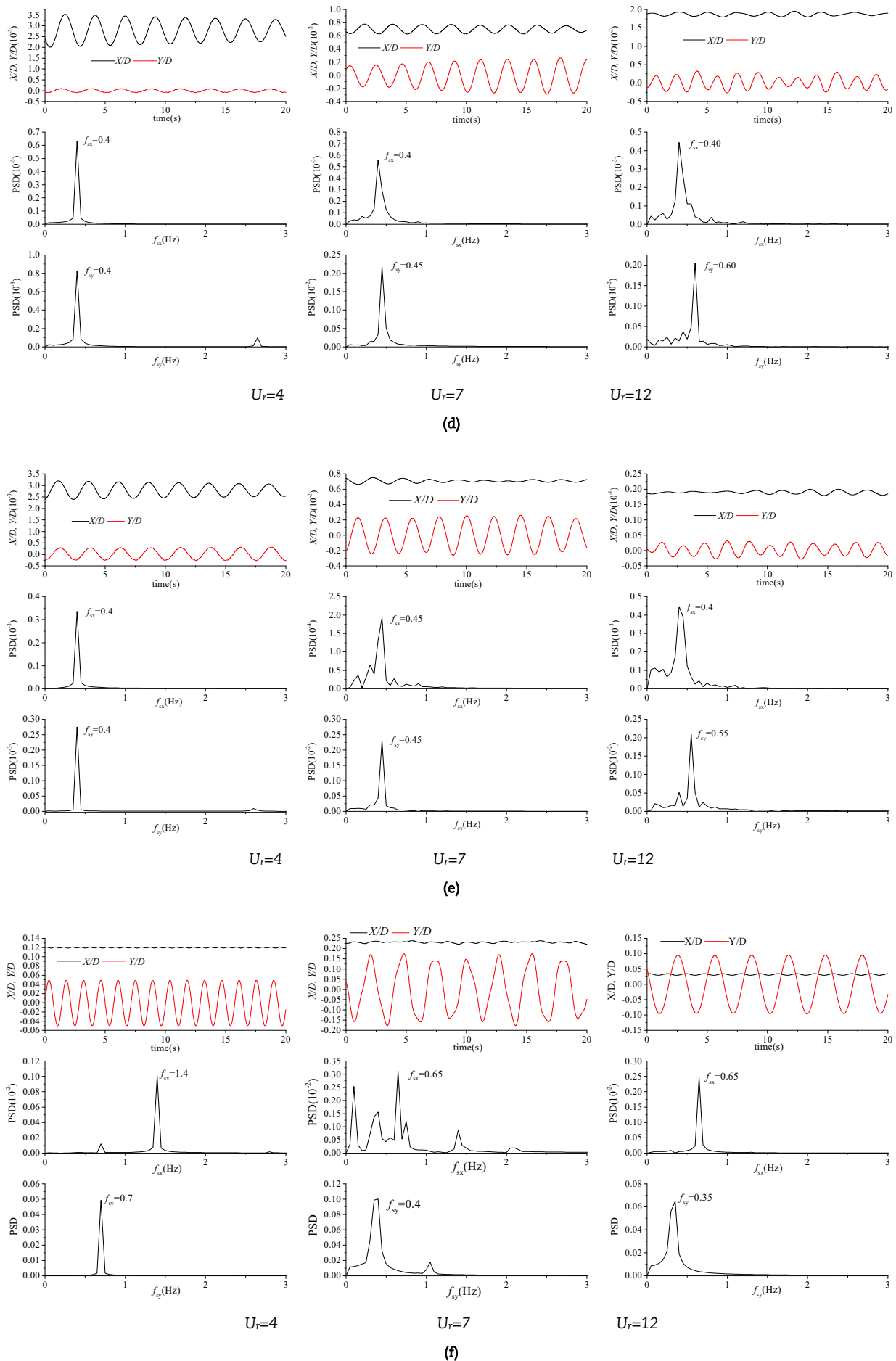


Fig. 6. Continued.



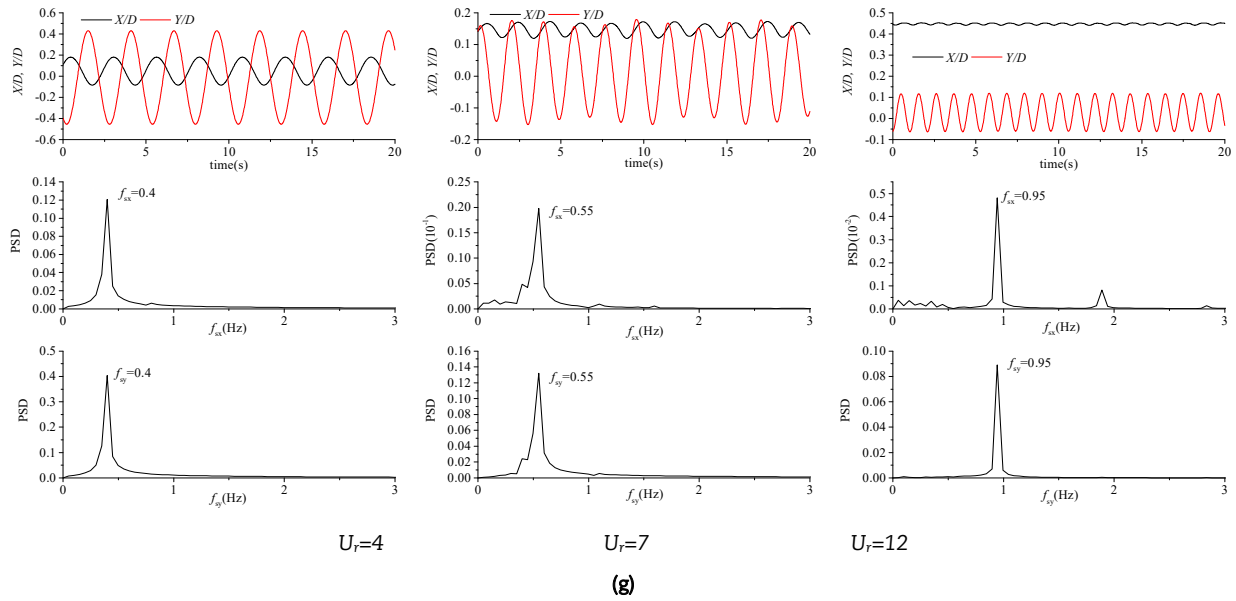


Fig. 6. Continued.

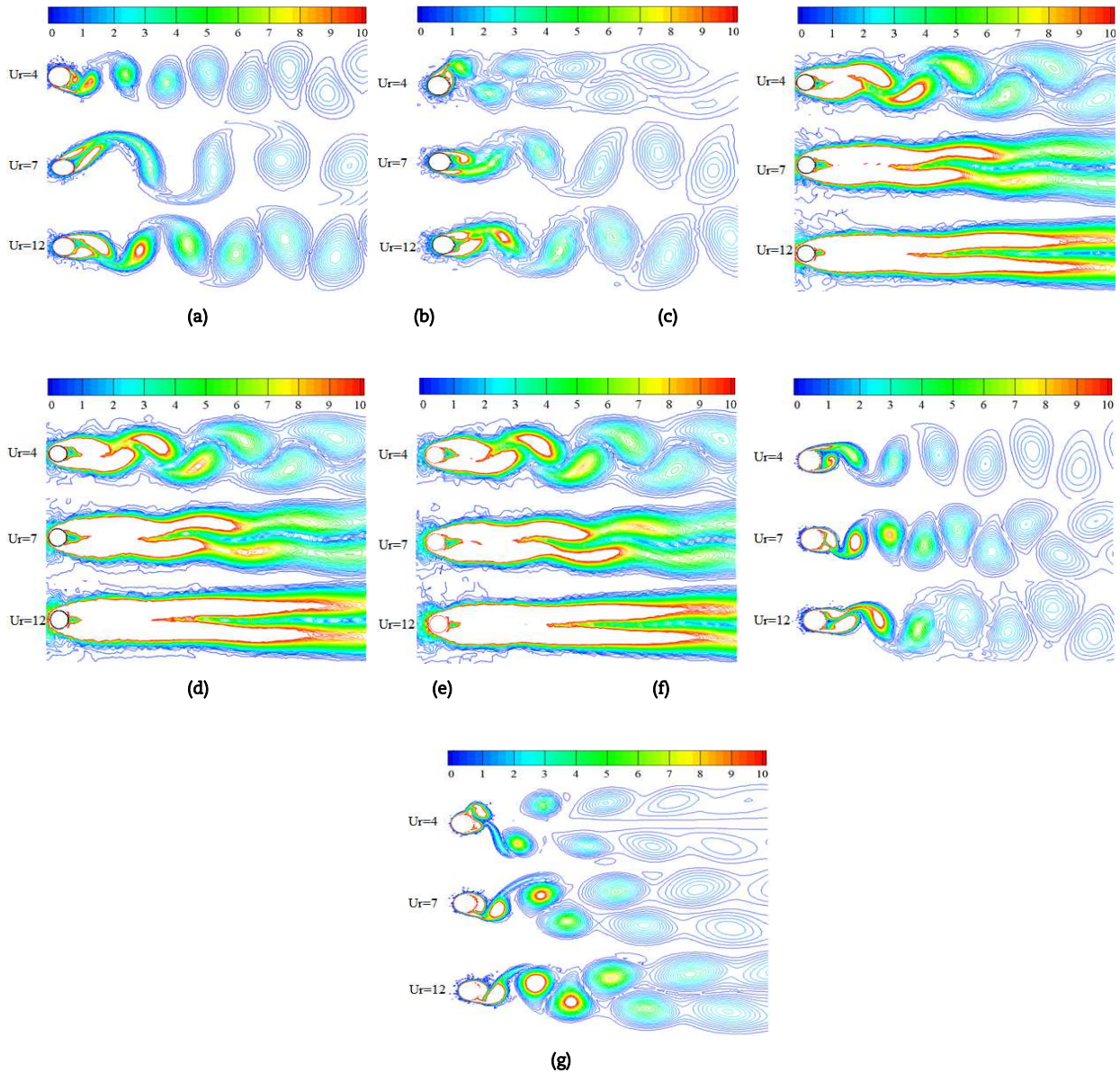


Fig. 7. Patterns of vortex shedding of cylinder in VIV for different number n of wavelike bumps: $n =$ (a) 0, (b) 1, (c) 3, (d) 5, (e) 7, (f) 9, and (g) 11.



3.4 Pattern of vortex shedding

Figure 7 shows the patterns of vortex shedding at the rear of the cylinder for different values of n . As can be seen, for $n=1$, the vortex-shedding pattern is 2P at $U_r=4$ and 12 and 2S at $U_r=7$. For $n=3, 5$, and 7 , the main vortex-shedding pattern is P+S and becomes chaotic gradually with increasing U_r . For $n=9$, the main vortex-shedding pattern is 2S, changing to P+S at $U_r=7$ and to 2P at $U_r=12$. For $n=11$, the main vortex-shedding pattern is 2P and becomes P+S with increasing U_r .

4. Conclusions

We used CFD to study how equipping a circular cylinder with wavelike bumps affected its VIV response, looking specifically at 1, 3, 5, 7, 9, and 11 wavelike bumps. We used the SST $k-\omega$ model, the RANS equations, and the Runge-Kutta method to investigate the self-oscillation of cylinder, and we draw the following conclusions:

- 1) The wavelike bumps suppressed the VIV to a certain degree, but that degree was not proportional to the number n of bumps. The suppression was most effective for $n=5$ or 7 , with a mitigation degree of 80% being reached in the resonance region. However, the suppression was poor for $n=11$, with the vibration being similar to that of the smooth cylinder ($n=0$) but marginally smaller in amplitude.
- 2) The smooth cylinder moved mainly on a figure-of-eight trajectory. With increasing n , the motion trajectory became elliptical shaped. However, before becoming that shape completely, it also had a “water droplet” shape and was relatively chaotic.
- 3) At a low reduced velocity U_r , the vortex-shedding pattern of the cylinder was mainly either 2S or 2P, changing gradually to P+S with increasing U_r . Finally, with further increase of U_r , the vortex-shedding pattern changes from 2S into 2P while 2P changes into 2S.

Author Contributions

Liping Tang planned the scheme, initiated the project, and suggested the method; Hong Yao and Zemin Huang have contributed in writing the manuscript and analyzed results; Liqi Wang has contributed in checking the result and revising the manuscript; Xiaohua Zhu planned the scheme and initiated the project together with Liping Tang. All authors discussed the results, reviewed, and approved the final version of the manuscript.

Acknowledgments

This research is supported by the National Natural Science Foundation of China (No. 51904262 and No. 51674214), the China Postdoctoral Science Foundation (No. 43XB3793XB), the State Scholarship Fund of the China Scholarship Council (No. 201808515055).

Conflict of Interest

The authors declared no potential conflicts of interest with respect to the research, authorship, and publication of this article.


References


- [1] Wu, X., Ge, F., Hong, Y., A review of recent studies on vortex-induced vibrations of long slender cylinders, *Journal of Fluids and Structures*, 28, 2012, 292-308.
- [2] Qu, Y., Metrikine, A.V., A single van der pol wake oscillator model for coupled cross-flow and in-line vortex-induced vibrations, *Ocean Engineering*, 196, 2020, 106732.
- [3] Williamson, C.H.K., Govardhan, R., A brief review of recent results in vortex-induced vibrations, *Journal of Wind Engineering and Industrial Aerodynamics*, 96(6-7), 2008, 713-735.
- [4] Drumond, G.P., Pasqualino, I.P., Pinheiro, B.C., Estefen, S.F., Pipelines, risers and umbilicals failures: A literature review, *Ocean Engineering*, 148, 2018, 412425.
- [5] Wang, Y., Gao, D., Recoil analysis of deepwater drilling riser after emergency disconnection, *Ocean Engineering*, 189, 2019, 106406.
- [6] Chang, Y., Zhang, C., Wu, X., Shi, J., Chen, G., Ye, J., Xu, L., Xue, A., A Bayesian network model for risk analysis of deepwater drilling riser fracture failure, *Ocean Engineering*, 181, 2019, 1-12.
- [7] Joshi, V., Jaiman, R.K., A variationally bounded scheme for delayed detached eddy simulation: application to vortex-induced vibration of offshore riser, *Computers & Fluids*, 157, 2017, 84-111.
- [8] Thorsen, M.J., Challabotla, N.R., Sævik, S., Nydal, O.J., A numerical study on vortex-induced vibrations and the effect of slurry density variations on fatigue of ocean mining risers, *Ocean Engineering*, 174, 2019, 1-13.
- [9] Fernandes, A.C., MirzaeiSefat, S., Cascão, L.V., Boas, P.V., Further investigation on vortex self induced vibration (VSIV), *Proceedings of the ASME 30th International Conference on Ocean, Offshore and Arctic Engineering*, Rotterdam, Netherlands, OMAE-2011-50187, 2011.
- [10] Fernandes, A.C., MirzaeiSefat, S., Cascão, L.V., Fundamental behavior of vortex self induced vibration (VSIV), *Applied Ocean Research*, 47, 2014, 183-191.
- [11] Song, L., Fu, S., Cao, J., Ma, L., Wu, J., An investigation into the hydrodynamics of a flexible riser undergoing vortex-induced vibration, *Journal of Fluids and Structures*, 63, 2016, 325-350.
- [12] Liu, C., Fu, S., Zhang, M., Ren, H., Time-varying hydrodynamics of a flexible riser under multi-frequency vortex-induced vibrations, *Journal of Fluids and Structures*, 80, 2018, 217-244.
- [13] Mazzilli, C.E.N., Sanches, C.T., Baracho, N., Odulpho G.P., Wiercigroch, M., Keber, M., Non-linear modal analysis for beams subjected to axial loads: analytical and finite-element solutions, *International Journal of Non-linear Mechanics*, 43(6), 2018, 551-561.
- [14] Pavlovskaja, E., Keber, M., Postnikov, A., Reddington, K., Wiercigroch, M., Multi-modes approach to modeling of vortex-induced vibration, *International Journal of Non-linear Mechanics*, 80, 2016, 40-51.
- [15] Chen, W., Li, M., Guo, S., Gan, K., Dynamic analysis of coupling between floating top-end heave and riser's vortex-induced vibration by using finite element simulations, *Applied Ocean Research*, 48, 2014, 1-9.
- [16] Kang, Z., Zhang, C., Chang, R., Ma, G., A numerical investigation of the effects of Reynolds number on vortex-induced vibration of the cylinders with different mass ratios and frequency ratios, *International Journal of Naval Architecture and Ocean Engineering*, 11(2), 2019, 835-850.
- [17] Lee, J., Bernitsas, M.M., High-damping, high-Reynolds VIV tests for energy harnessing using the VIVACE converter, *Ocean Engineering*, 38(16), 2011, 1697-1712.
- [18] Chen, W., Ji, C., Xu, D., Zhang, Z., Vortex-induced vibrations of two inline circular cylinders in proximity to a stationary wall, *Journal of Fluids and Structures*, 94, 2020, 102958.
- [19] Chung, M.H., Transverse vortex-induced vibration of spring-supported circular cylinder translating near a plane wall, *European Journal of Mechanics B-fluids*, 55, 2016, 88-103.
- [20] Manuel, J., Barbosa, D.O., Qu, Y., Metrikine, A.V., Lourens, E.M., Vortex-induced vibrations of a freely vibrating cylinder near a plane boundary: experimental investigation and theoretical modeling, *Journal of Fluids and Structures*, 69, 2017, 382-401.



- [21] Munir, A., Zhao, M., Wu, H., Lu, L., Effects of gap ratio on flow-induced vibration of two rigidly coupled side-by-side cylinders, *Journal of Fluids and Structures*, 91, 2019, 102726.
- [22] Daneshvar, S., Morton, C., On the vortex-induced vibration of a low mass ratio circular cylinder near planar boundary, *Ocean Engineering*, 201, 2020, 107109.
- [23] Kang, Z., Jia, L., An experiment study of a cylinder's two degree of freedom VIV trajectories, *Ocean Engineering*, 70, 2013, 129-140.
- [24] Meliga, P., Chomaz, J.M., Gallaire, F., Extracting energy from a flow: an asymptotic approach using vortex-induced vibrations and feedback control, *Journal of Fluids and Structures*, 27(5-6), 2011, 861-874.
- [25] Jiménez-González, J.I., Huera-Huarte, F.J., Experimental sensitivity of vortex-induced vibrations to localized wake perturbations, *Journal of Fluids and Structures*, 74, 2017, 53-63.
- [26] Banafsheh S.A., Yahya M.S., An experimental study to investigate the validity of the independence principle for vortex-induced vibration of a flexible cylinder over a range of angles of inclination, *Journal of Fluids and Structures*, 78, 2018, 343-355.
- [27] Franzini, G.R., Pesce, C.P., Goncalves, R.T., Fajarra, A.L.C., Mendes, P., An experimental investigation on concomitant vortex-induced vibration and axial top-motion excitation with a long flexible cylinder in vertical configuration, *Ocean Engineering*, 156, 2018, 596-612.
- [28] Borges, F.C.L., Roitman, N., Magluta, C., Castello, D.A., Franciss, R., A concept to reduce vibrations in steel catenary risers by the use of viscoelastic materials, *Ocean Engineering*, 77, 2014, 1-11.
- [29] Gao, Y., Yang, J., Xiong, Y., Wang, M., Peng, G., Experimental investigation of the effects of the coverage of helical strakes on the vortex-induced vibration response of a flexible riser, *Applied Ocean Research*, 59, 2016, 53-64.
- [30] Hong, K.S., Shah, U.H., Vortex-induced vibrations and control of marine risers: a review, *Ocean Engineering*, 152, 2018, 300-315.
- [31] Wang, W., Song, B., Mao, Z., Tian, W., Zhang, T., Han, P., Numerical investigation on vortex-induced vibration of bluff bodies with different rear edges, *Ocean Engineering*, 197, 2020, 106871.
- [32] Korkischko, I., Meneghini, J.R., Experimental investigation of flow-induced vibration on isolated and tandem circular cylinders fitted with strakes, *Journal of Fluids and Structures*, 26(4), 2010, 611-625.
- [33] Zhu, H., Zhao, Y., Hu, J., Performance of a novel energy harvester for energy self-sufficiency as well as a vortex-induced vibrations suppressor, *Journal of Fluids and Structures*, 91, 2019, 102736.
- [34] Nikoo, H.M., Bi, K., Hao, H., Textured pipe-in-pipe system: a compound passive technique for vortex-induced vibration control, *Applied Ocean Research*, 95, 2020, 102044.
- [35] Zhu, H., Yao, J., Ma, Y., Zhao, H., Tang, Y., Simultaneous CFD evaluation of VIV suppression using smaller control cylinders, *Journal of Fluids and Structures*, 57, 2015, 66-80.
- [36] Wanderley, J.B.V., Souza, G.J.B., Sphaier, S.H., Levi, C., Vortex-induced vibration of an elastically mounted circular cylinder using an upwind TVD two-dimensional numerical scheme, *Ocean Engineering*, 35(14-15), 2008, 1533-1544.
- [37] Rahmanian, M., Zhao, M., Cheng, L., Zhou, T., Two-degree-of-freedom vortex-induced vibration of two mechanically coupled cylinders of different diameters in steady current, *Journal of Fluids and Structures*, 35, 2012, 133-159.
- [38] Jauvtis, N., Williamson, C.H.K., Vortex-induced vibration of a cylinder with two degrees of freedom, *Journal of Fluids and Structures*, 17(7), 2003, 1035-1042.

ORCID iD

Liping Tang  <https://orcid.org/0000-0003-0981-2120>

Xiaohua Zhu  <https://orcid.org/0000-0002-0507-3773>



© 2021 Shahid Chamran University of Ahvaz, Ahvaz, Iran. This article is an open access article distributed under the terms and conditions of the Creative Commons Attribution-NonCommercial 4.0 International (CC BY-NC 4.0 license) (<http://creativecommons.org/licenses/by-nc/4.0/>).

How to cite this article: Tang L., Huang Z., Wang L., Zhu X. How Wavelike Bumps Mitigate the Vortex-induced Vibration of a Drilling Riser, *J. Appl. Comput. Mech.*, 7(3), 2021, 1413–1424. <https://doi.org/10.22055/JACM.2021.34951.2527>

Publisher's Note Shahid Chamran University of Ahvaz remains neutral with regard to jurisdictional claims in published maps and institutional affiliations.

